Simulated Frequency Dependence of Radar Observations of Tornadoes

DAVID J. BODINE

Advanced Study Program, National Center for Atmospheric Research,[a] Boulder, Colorado, and School of Meteorology, and Advanced Radar Research Center, University of Oklahoma, Norman, Oklahoma

ROBERT D. PALMER

School of Meteorology, and Advanced Radar Research Center, University of Oklahoma, Norman, Oklahoma

TAKASHI MARUYAMA

Disaster Prevention Research Institute, Kyoto University, Kyoto, Japan

CALEB J. FULTON, YE ZHU, AND BOON LENG CHEONG

Advanced Radar Research Center, and School of Electrical and Computer Engineering, University of Oklahoma, Norman, Oklahoma

(Manuscript received 15 May 2015, in final form 28 June 2016)

ABSTRACT

To obtain accurate radar-measured wind measurements in tornadoes, differences between air and Doppler velocities must be corrected. These differences can cause large errors in radar estimates of maximum tangential wind speeds, and large errors in single-Doppler retrievals of radial and vertical velocities. Since larger scatterers (e.g., debris) exhibit larger differences from air velocities compared to small scatterers (e.g., raindrops), the dominant scatterer type affecting radar measurements is examined. In this study, radar variables are simulated for common weather radar frequencies using debris and raindrop trajectories computed with a large-eddy simulation model and two electromagnetic scattering models. These simulations include a large range of raindrop and wood board sizes and concentrations, and reveal the significant frequency dependence of the equivalent reflectivity factor and Doppler velocity. At S band, dominant scatterers are wood boards, except when wood board concentrations are very low. In contrast, raindrops are the dominant scatterers at Ka and W bands even when large concentrations of wood boards are present, except for low raindrop concentrations. Dual-wavelength velocity differences exhibit high correlation with air and Doppler velocity differences for most cases, which may enable direct measurements of scatterer-induced Doppler velocity bias in tornadoes. Moreover, dual-wavelength ratios are shown to exhibit strong correlations with dominant scatterer size, except when Rayleigh scatterers are dominant. Finally, vertical velocity retrievals are shown to exhibit lower errors at high frequencies, and large errors remain at centimeter wavelengths even after debris centrifuging corrections are applied in cases with high debris concentration.

1. Introduction

Radars measure scatterers' velocities rather than air velocities, resulting in measurement errors when Doppler radial velocities (herein called Doppler velocities) are used to estimate tornado wind speeds. In tornadoes, scatterers include both debris and hydrometeors. Snow (1984) and Dowell et al. (2005) show that debris is centrifuged outward relative to the air, and Dowell et al. (2005) also showed that tangential and vertical velocities of debris are reduced relative to the airspeed. Simulations by Dowell et al. (2005) showed that differences between air and scatterer velocities can reach tens of meters per second for larger scatterers, and velocity differences increase for smaller tornado diameters and higher tangential velocities. Finally, Doppler velocity measurements for a single scatterer type represent a mass-weighted average, and thus portions of the resolution volume with

[a] The National Center for Atmospheric Research is sponsored by the National Science Foundation.

Corresponding author address: David Bodine, Advanced Study Program, National Center for Atmospheric Research, 3450 Mitchell Lane, Boulder, CO 80302.
E-mail: dbodine@ucar.edu

DOI: 10.1175/JTECH-D-15-0120.1

© 2016 American Meteorological Society

higher debris concentrations have a greater contribution to Doppler velocity measurements (Lewellen et al. 2008).

Because large differences between air and scatterer velocities occur in tornadoes, these differences must be corrected in Doppler velocity measurements to obtain accurate wind measurements. Given strong scientific interest in understanding near-surface wind speeds (e.g., to assess societal impacts or understand corner flow structure), mitigating debris centrifuging errors close to the ground remains a critical yet elusive goal. Large debris concentrations are highest near the surface (e.g., Wurman et al. 1996; Wurman and Gill 2000; Dowell et al. 2005), leading to the largest differences between air and scatterer velocities. As a result, near-surface radial divergence is often observed in Doppler radar observations (Wurman and Gill 2000; Dowell et al. 2005; Wakimoto et al. 2012), whereas laboratory experiments and numerical simulations exhibit converging flow. Near-surface radial divergence leads to further errors when vertical velocity retrievals are performed, such as the ground-based velocity tracking display (GBVTD; Lee et al. 1999). In Nolan (2013) it was shown that anomalously strong retrieved downdrafts result from increased radial divergence caused by debris centrifuging.

To address the debris centrifuging bias problem, Wakimoto et al. (2012) propose a technique to correct debris centrifuging bias by assuming the scatterers in the tornado are raindrops, and then calculating a median diameter based on radar reflectivity factor. For a tornado case without large visible debris, their analysis showed that divergent near-surface radial flow became convergent after the debris centrifuging correction was applied to the GBVTD, resulting in a more realistic wind field. A limitation to this technique is that the dominant scatterers must be raindrops or small objects with similar electromagnetic and aerodynamic characteristics, otherwise the correction is underestimated. Polarimetric radar observations of tornado debris signatures (TDSs) frequently reveal areas of low copolar cross-correlation coefficient (ρ_{hv}) at S band (Ryzhkov et al. 2005; Kumjian and Ryzhkov 2008; Bodine et al. 2013), C band (Palmer et al. 2011; Schultz et al. 2012a,b), and X band (Bluestein et al. 2007; Snyder and Bluestein 2014), suggesting that the Rayleigh assumption does not apply in such cases. Thus, the raindrop scattering assumption requires further testing.

Two important questions must be addressed to estimate and correct debris centrifuging errors. First, physical scatterer attributes must be determined (sizes, concentrations). Second, if the scatterer(s) characteristics are known, then its impact on the backscattered radar signal must be quantified. Because scatterer types may vary significantly among different tornado cases or throughout a tornado's lifetime, significant uncertainty exists in determining scatterer type. In some cases, visual observations may corroborate the presence or absence of certain debris types, but debris may be obscured (e.g., by debris clouds or precipitation). Radar observations have the potential to provide information about debris characteristics; however, such inferences to date have been primarily qualitative.

In the present study, experiments are performed to simulate radar observations of tornadoes at multiple frequencies using a large-eddy simulation (LES) model, and to examine how Rayleigh and Mie scatterers affect radar measurements. Several simplified assumptions are made for debris types considered to focus this large parameter space. Tornadoes loft different types of debris from natural surfaces (e.g., grass, leaves, soil, rocks) and man-made structures, including wood boards, insulation, and roof tiles (e.g., Snow et al. 1995; McDonald et al. 2004). In this study we focus on two types of scatterers, wood boards and raindrops, and assume a steady debris source. The electromagnetic models assume simplified shapes of wood boards (spheres and square plates). Since actual wood debris has a wide range of aspect ratios or shapes (e.g., 2 in. × 4 in. wood lumber or 4 ft. × 8 ft. plywood sheets), comparisons of two different shapes help examine the importance of debris shape to radar observations. Debris is also assumed to be randomly oriented based on differential reflectivity (Z_{DR}) near 0 dB in TDSs (Ryzhkov et al. 2005; Bodine et al. 2013), which indicate that debris has random orientations (in a mean sense). Finally, the analysis examines one tornado vortex flow, so future studies should consider different tornado flows.

Simulations reveal the significant frequency dependence of radar variables. Based on these simulations, recommendations for estimating and mitigating velocity errors associated with debris centrifuging and extracting information about debris characteristics are presented. The primary goals of this study are as follows:

- Examine the frequency dependence of the equivalent reflectivity factor and Doppler velocity.
- Explore the potential of dual-frequency variables for assessing scatterer size.
- Develop dual-frequency methods to estimate differences in air and radar-measured velocities.

Section 2 describes the LES model and trajectory calculations. Then, radar variable simulations are discussed, including the electromagnetic models used for debris and raindrops. In section 3, experiments with varying rain and debris concentrations are performed to examine the frequency dependence of the equivalent reflectivity factor (Z_e) and Doppler velocity. Conclusions are presented in section 4.

TABLE 1. List of LES model configuration parameters for the vortex breakdown simulation for a nondimensional simulation with a characteristic velocity of 1 m s^{-1}.

Model configuration parameters	
Inflow region length (l_{inf})	0.23 m
Mean radius to inflow region (r_{inf})	0.75 m
Convergence region height (h_{cvg})	0.15 m
Inflow boundary velocity (v_{in})	0.04 m s^{-1}
Horizontal domain length (l_{dom})	1.22 m
Convection region radius (r_{cvt})	0.6 m
Updraft opening radius (r_{up})	0.15 m
Top outlet radius (r_{top})	0.15 m
Convection region height (h_{cvt})	0.76 m
Top outlet velocity (w_{top})	0.13 m s^{-1}
$h_{\mathrm{cvg}}/r_{\mathrm{up}}$	1.0
$h_{\mathrm{cvt}}/h_{\mathrm{cvg}}$	5.1
$r_{\mathrm{inf}}/r_{\mathrm{up}}$	5.0

2. Radar variable simulations using the LES model

In this section, the LES model used to generate the tornadolike flow and calculate scatterer trajectories is discussed. Then, methods used to simulate Z_e and Doppler velocity at different radar frequencies are presented.

a. LES model and trajectory calculations

The LES model used in this study (Uchida and Ohya 2003; Maruyama 2011) simulates the flow of a vortex chamber (Davies-Jones 1973; Church et al. 1979), producing a wide range of tornado-like flows. The reader is referred to Maruyama (2011) and Bodine (2014) for more details about the numerical calculation scheme of the LES model, but a brief discussion is presented here. The LES model configuration parameters are provided in Table 1. The model domain is divided into two primary regions: convergence and convection regions (Fig. 1). Convergence and convection region heights, h_{cvg} and h_{cvt}, respectively, exhibit a ratio consistent with tornado vortex chambers and expected values in nature (Church et al. 1979). The convergence and convection regions are separated by an updraft hole radius of r_{up}. Inflow into the vortex chamber is provided through four inlet regions of length, l_{inf}, with an inflow velocity of v_{in}. The top outlet hole has a radius of r_{top} and updraft velocities of w_{top}. The model is nondimensional, so a characteristic velocity, V_0, is used to provide dimensional scaling. In this study, V_0 is 225 m s^{-1}.

In the LES model, 155, 155, and 79 grid points are used in the x, y, and z dimensions, respectively. A constant horizontal grid spacing is used within the updraft radius r_{up} of 15 m, and a stretched horizontal grid is used at greater radii with horizontal grid spacing ranging from 15 to 155 m. The vertical grid is also stretched from 15 to 93 m with values between 15 and 30 m in the convergence region. Lower boundary conditions are semi-slip with a surface roughness length of 0.03 m. On other simulator surfaces (e.g., sidewalls and the plate between convergence and convection regions), no-slip boundary conditions are employed. Using these boundary conditions and the configuration specified in Table 1, a vortex breakdown simulation is produced. Mean axisymmetric radial, tangential, and vertical velocities are shown in Figs. 2a–c, respectively. Maximum mean tangential wind speed of 72 m s^{-1} occurs at a radius of 54 m and a height of 32 m.

Using wind data from the vortex breakdown simulation, raindrop and debris trajectories are computed using second-order Runge–Kutta integration to solve the following scatterer trajectory equation:

$$\frac{du_i}{dt} = C_D T_a (u_i - u_{di})|u_i - u_{di}| - \delta_{i,3}, \tag{1}$$

where u_i is the air velocity and u_{di} is scatterer velocity. The term T_a is the Tachikawa number (Holmes et al. 2006), defined as

$$T_a = \frac{\rho A V_0^2}{2mg}, \tag{2}$$

where ρ is air density, A is scatterer area, V_0 is a characteristic velocity, m is scatterer mass, and g is gravitational acceleration. The term T_a represents a ratio of aerodynamic to gravitational forces and is a nondimensional parameter that determines trajectories of different scatterer types. For nearly spherical scatterers (i.e., raindrops herein), C_D varies as a function of the particle Reynolds number (Re_p) based on an empirical formula from White (1991):

$$C_D \approx \frac{24}{\mathrm{Re}_p} + \frac{6}{1 + \sqrt{\mathrm{Re}_p}} + 0.4. \tag{3}$$

For wood boards, a constant drag force coefficient of 2 is employed for a square plate (Simiu and Scanlan 1996), such as a plywood sheet. Trajectory calculations were tested in Bodine (2014), and results similar to Dowell et al. (2005) were obtained for radial, tangential, and vertical velocities for idealized vortices.

Two scatterer types are simulated in the present study: raindrops and square wood plates. Raindrop trajectories are computed for the following diameters: 0.5, 1, 1.5, 2, and 4 mm. For each drop size, 1 million trajectories are calculated to provide a sufficient number of trajectories for stable scatterer concentration and velocity statistics. However, because of computational constraints, it is not

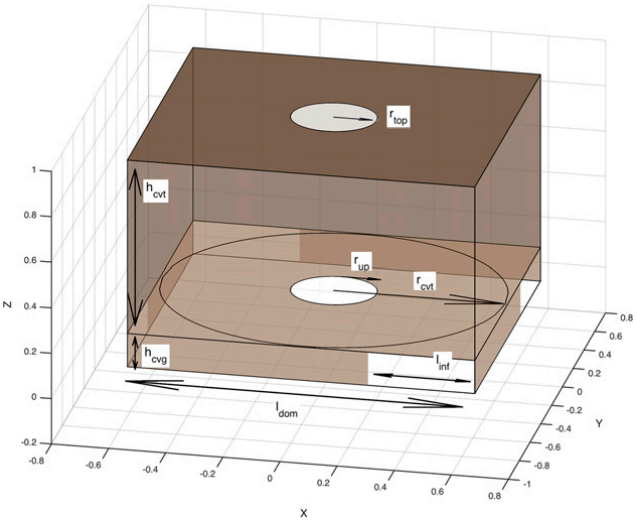

FIG. 1. Configuration of the LES model for a vortex breakdown simulation (the axes shown are dimensionless). The vortex chamber is divided into convergence and convection regions (light and dark brown shading, respectively), and the two regions are separated by a plate with r_{up}. Flow into the convergence region enters through four inlets on the sidewalls with l_{inf} and h_{cvg}. Flow exits the model domain through the outlet at the top with r_{top}.

feasible to explicitly simulate all trajectories required for a drop size distribution (DSD) with a high number concentration (e.g., hundreds or thousands of drops per cubic meter). Thus, we employ a scaling factor S_i so that each drop represents S_i drops. Accordingly, a much larger number of drops can be simulated in the domain as long as accurate statistics for debris concentration and velocity are obtained. The scaling factors used for each drop size are presented in Table 2. The scaling factors are weighted by a Marshall–Palmer distribution (Marshall and Palmer 1948) with a rain rate of $20\,\mathrm{mm\,h^{-1}}$. Finally, raindrops are initialized randomly within the domain.

For square wood boards, 1000 trajectories per size are computed for 10 different sizes with uniformally distributed lengths (l) between 41.6 and 415.7 mm and thicknesses of $(1/20)l$. Wood boards are initialized randomly within the lowest two grid cells where $w > 10\,\mathrm{m\,s^{-1}}$ to provide more realistic debris lofting.[1] After a raindrop or wood board hits the surface or exits the simulation domain, a new trajectory is reinitialized. LES mean scatterer concentrations and velocities used in forthcoming radar variable simulations are computed over a 5740-s period with the aforementioned fixed number of trajectories.

b. Radar variable simulations

To compute radar variables using electromagnetic scattering calculations, raindrop and wood board concentrations and velocities from the LES model are axisymmetrically averaged to a radial grid spacing of 30 m, while the model vertical grid spacing is retained. Radar resolution volume dimensions are often larger than 30 m, particularly at lower frequencies (e.g., S band). However, the primary purpose of this manuscript is to examine the frequency dependence of radar observations, and thus a common grid is selected to facilitate comparisons among different frequencies. For dual-frequency radar observations without spatiotemporally matched radar resolution volumes (e.g., noncollocated radars or collocated radars with different antenna patterns), the frequency dependence of radar observations may differ because scatterer characteristics and positions within the two radars' resolution volumes differ. Thus, dual-frequency simulations herein most closely represent radar observations from a matched beam radar system, such as the National Center for Atmospheric Research (NCAR) S-PolKa radar (Vivekanandan et al. 2004).

Two types of electromagnetic scattering calculations are presented for comparison, transmission (T; Waterman 1969, 1971) matrix calculations and physical optics approximations (POA). T-matrix calculations are commonly used to compute radar variables for hydrometeors and provide accurate values for spheroids. However, T-matrix calculations often fail to converge for scatterers with large eccentricities, high refractive indices, or very large scatterer sizes. Thus, T-matrix calculations are applicable only to a subset of idealized debris types (spheroids) and cannot account for irregularities in debris shapes (e.g., sharp edges). In spite of these limitations, Bodine et al. (2014b) found that T-matrix-derived Z_e for debris exhibits similar characteristics to observed dual-wavelength horizontal radar reflectivity factor (Z_{HH}) differences from the 10 May 2010 Moore–Oklahoma City, Oklahoma, tornado.

The POA model enables calculations of backscatter cross sections (σ_b) for more realistic debris shapes compared to T-matrix calculations. The term σ_b is computed using the POA model for wood boards with l ranging from 41.6 to 415.7 mm and thicknesses of $(1/20)l$, which have the same volume as wood spheres used in the T-matrix calculations.

Using backscatter amplitudes from T-matrix calculations and mean σ_b from the POA model (discussed shortly), Z_e is computed. Backscatter amplitudes are computed using Fortran T-matrix codes described in

[1] To our knowledge, debris lofting characteristics in tornadoes have not been studied or quantified (e.g., initial vertical velocities); thus, debris is lofted only where vertical velocities are sufficiently intense to loft wood boards.

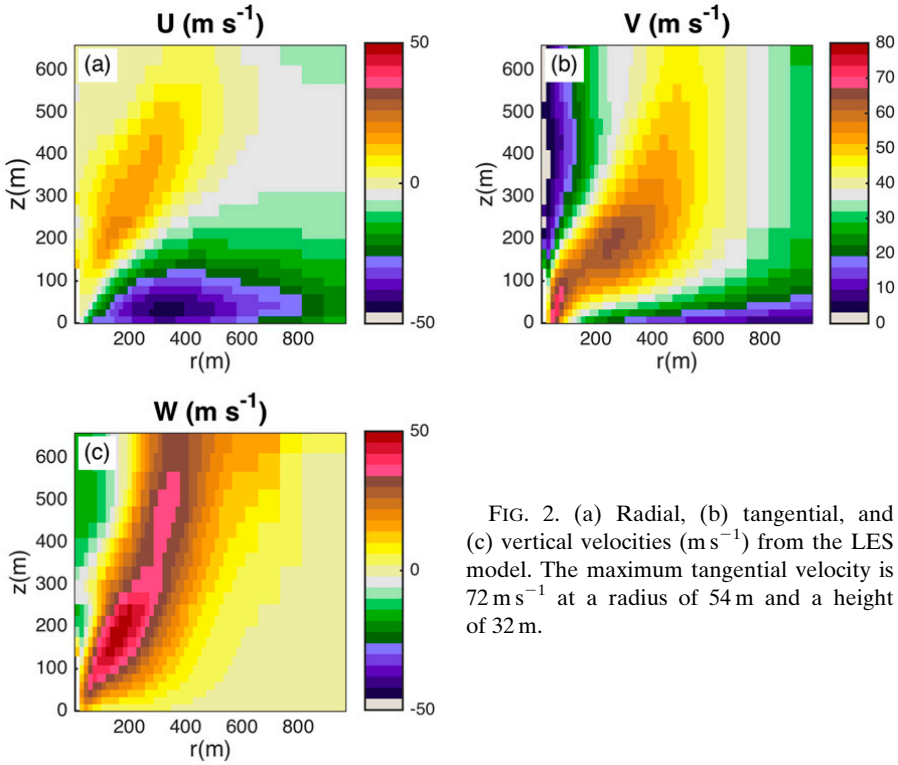

FIG. 2. (a) Radial, (b) tangential, and (c) vertical velocities ($\mathrm{m\,s^{-1}}$) from the LES model. The maximum tangential velocity is $72\,\mathrm{m\,s^{-1}}$ at a radius of 54 m and a height of 32 m.

Mishchenko et al. (1996) and Mishchenko (2000). From T-matrix calculations, Z_e is computed for rain and debris as follows:

$$Z_e = \frac{4\lambda^4}{\pi^4|K_w|^2}\int_{D_{\min}}^{D_{\max}} |s(D,\epsilon_r)|^2 N(D)\,dD, \qquad (4)$$

where ϵ_r is the complex relative permittivity, λ is the radar wavelength, s is the backscatter amplitude, and K_w is a function of the refractive index of water (Doviak and Zrnić 1993). The term $N(D)$ is the scatterer size distribution, and D is the scatterer diameter. Debris is simulated over a large range of sizes and frequencies, so spherical shapes are used in the T-matrix calculations to enable convergence. The term ϵ_r for raindrops is computed based on Eqs. (5) and (6) of Ray (1972), and ϵ_r of dry wood boards are obtained from Daian et al. (2006) and Jebbor et al. (2011) with a value of 2–0.2j. Additionally, calculations were performed for wet boards (20% water content) with an ϵ_r of 4.65–1.46j based on Ulaby and El-Rayes (1986) and Senior et al. (1987). Unfortunately, ϵ_r for wood boards have only been measured at S and X bands, and thus some uncertainty exists in their applicability at other wavelengths. A comprehensive investigation of ϵ_r for common debris types is needed but that is beyond the scope of this study. For mean σ_b data, Z_e is computed using

$$Z_e = \frac{\lambda^4}{\pi^5|K_w|^2}\int_0^{\infty} \sigma_b(D)N(D)\,dD. \qquad (5)$$

Mean σ_b is computed using the POA model for each square wood board size by averaging σ_b over a discrete set of incidence angles that are uniformly distributed

TABLE 2. Drop diameters and S_i used to compute the equivalent reflectivity factor and Doppler velocity. The total number of drops in the simulation domain is the scaling factor multiplied by the number of trajectories. The scaling factor is weighted by a Marshall–Palmer DSD with a rain rate of $20\,\mathrm{mm\,h^{-1}}$.

Drop diameter (mm)	Low drop concentration S_i	Moderate drop concentration S_i	High drop concentration S_i
0.5	3.36×10^3	3.36×10^4	3.36×10^5
1	5.38×10^2	5.38×10^3	5.38×10^4
1.5	1.84×10^2	1.84×10^3	1.84×10^4
2	85.1	851	8.51×10^3
4	5.9	59.2	5.92×10^2

over a far-field sphere, with sufficient angular resolution to ensure convergence of the resulting mean value. This requires a larger number of points for larger objects at higher frequencies. Each radar cross section (RCS) is derived from a POA, where the scattered fields are calculated based on truncated equivalent currents on the near side of the board. These currents are derived from oblique incidence plane wave reflection coefficients derived either from the approximate formulation in Senior et al. (1987) for thin wood boards (less than a few tenths of a λ in thickness) or on a full two-way plane wave expansion inside of electrically thicker boards [see sections 5.5.2.D and 11.3.2 in Balanis (2012)]. In both techniques, conductive and dielectric losses are carefully taken into account, but the weaker edge diffraction effects are not.

The value of Z_e for wood boards computed from T-matrix calculations and the POA model are shown in Fig. 3 for a concentration of $1\,\mathrm{m}^{-3}$. POA Z_e is shown for both dry (asterisks) and wet wood boards (circles). For the dry wood board calculations, mean Z_e averaged over all diameters is greater for the POA model compared to T-matrix calculations by 0.8–7.4 dB. Atlas (1953) found that mean σ_b for prolate or oblate spheroidal ice particles was greater than mean σ_b for an equivalent volume sphere, and a similar effect is observed here for wood boards. For a flat plate, specular reflection occurs when the plate is aligned normally to the incident electromagnetic wave and enhances mean σ_b particularly at higher frequencies (Knott et al. 1993). Finally, since tornadoes can entrain large concentrations of raindrops and wood boards may contain some moisture content, the impact of changing the wood boards' water content on Z_e is considered. For the wet boards, mean Z_e increases by 6.2–7.8 dB for S–W bands, which is consistent with an approximate doubling of ϵ_r.

Large dual-wavelength Z_e differences, often called dual-wavelength ratios (DWRs) or dual-frequency ratios (DFRs), are evident for all frequency pairs (Fig. 3). S–C-band and S–X-band DWRs are on the order of 10 and 20 dB, respectively, which are similar to DWRs observed for hail (e.g., Atlas and Ludlam 1961; Snyder et al. 2010; Picca and Ryzhkov 2012) and debris (Bodine et al. 2014b). Between S and W bands, wood plates can produce DWRs exceeding 60 dB. DWRs are also similar for both dry and wet wood boards, since all frequencies exhibit a similar increase in Z_e after wetting.

The value for Z_e for raindrops is shown in Fig. 4 for common weather radar frequencies. DWRs in rain among centimeter wavelengths are much smaller compared to debris, and thus DWRs among S, C, or X bands could help ascertain whether rain or debris is present. Small differences at centimeter wavelengths occur as a consequence of different ϵ_r, and Mie scattering effects at C and X bands for larger diameters. In contrast, Z_e in rain at Ka and W bands is much lower compared to centimeter wavelengths as a consequence of Mie scattering. Between S and W bands, large drops can produce DWRs of 40–50 dB.

Electromagnetic scattering differences among radar frequencies impact Doppler velocity measurements because mean Doppler velocity $\overline{v}(r_0)$ is a function of individual scatterers' velocities $v_p(r_1)$ weighted by their reflectivities $\eta(r_1)$ and illumination functions (Doviak and Zrnić 1993), as follows:

$$\overline{v}(r_o) = \frac{\iiint v_p(r_1)\eta(r_1)I(r_0, r_1)\,dV_1}{\iiint \eta(r_1)I(r_0, r_1)\,dV_1}, \tag{6}$$

where the resolution volume center range is r_o and the scatterers' range is r_1. The illumination function weights the scatterers' σ_b (e.g., due to the antenna or range weighting function). Based on Eq. (6), it is evident that scatterers with large reflectivities or high number concentrations will have a greater impact on Doppler velocity measurements.

Mean reflectivity-weighted velocity is used to approximate Doppler velocity [Eq. (6)], and this approximation generates good results if scatterers are uniformally distributed throughout the resolution volume and are present in relatively high concentrations. Herein mean reflectivity-weighted radial and tangential velocities are referred to as u_{dr} and v_{dr}, respectively, and radial and tangential air velocities are referred to as U and V, respectively. The radial and tangential velocity measurement errors, associated with assuming the radar measures air velocity, are $u_{\mathrm{dr}} - U$ and $v_{\mathrm{dr}} - V$, respectively. Future studies could employ a realistic radar simulator (e.g., Cheong et al. 2008, 2015) to examine how radar resolution volume size, attenuation, sidelobes, nonuniform debris distributions, etc., affect radar measurements in tornadoes at different frequencies.

Dual-frequency velocity differences will also be computed to assess their potential for estimating Doppler velocity errors. Radial (DDU) and tangential (DDV) dual-frequency velocity differences will be computed and will represent the velocity difference measured by an idealized dual-frequency radar (i.e., matched beam radar system). *Radial* dual-frequency velocity differences (DDU) correspond to simulated dual-frequency velocity differences where the radar beam aligns with radial scatterer motion (e.g., a range–height indicator scan through the vortex center). This is represented as follows:

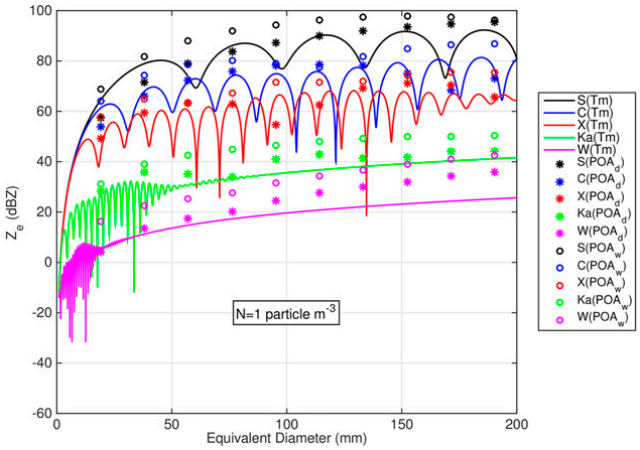

FIG. 3. Plot of Z_e (dBZ) for wood boards at S, C, X, Ka, and W bands with a concentration of 1 m^{-3}. Term Z_e from T-matrix calculations for dry wood boards is shown with solid lines, and the POA model Z_e is shown with asterisks for dry wood boards and circles for wet wood boards. For both methods, Z_e varies by approximately 60 dB between S and W bands.

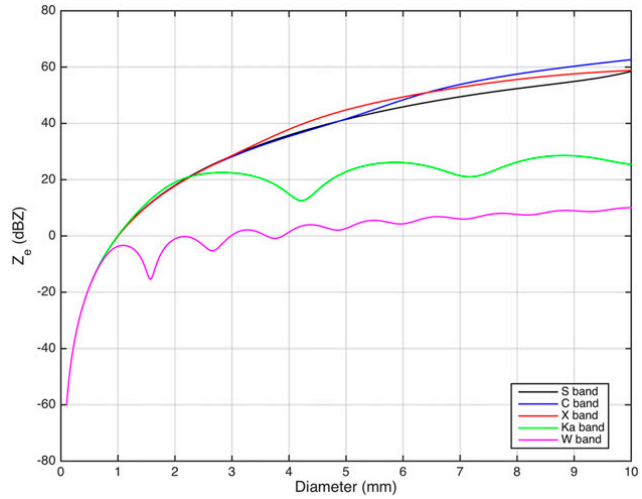

FIG. 4. Plot of T-matrix Z_e (dBZ) for raindrops at S, C, X, Ka, and W bands for a concentration of 1 m^{-3}. For large raindrops, dual-frequency Z_e differences can approach 40 dB for the largest expected drop sizes (e.g., about 8-mm diameters).

$$\mathrm{DDU} = u_{\mathrm{dr}}(f_2) - u_{\mathrm{dr}}(f_1), \tag{7}$$

where f_1 and f_2 are the two radar frequencies. Likewise, DDV is computed using

$$\mathrm{DDV} = v_{\mathrm{dr}}(f_2) - v_{\mathrm{dr}}(f_1), \tag{8}$$

and represents the simulated dual-frequency velocity difference where the radar beam aligns with tangential scatterer motion. In a different application, dual-frequency velocity differences have been applied to sizing of ice crystals for vertically pointing radars at Ka and W bands (Matrosov 2011), and greater dual-frequency velocity differences were associated with ice particle size distributions with smaller slope parameters (i.e., larger median volume particle sizes). Differential velocity has also been computed in tornadoes using (single frequency) polarimetric radars by taking a velocity difference between the horizontal and vertical polarizations (Snyder and Bluestein 2014). In this study, they found that higher velocity differences between polarizations occurred in resolution volumes with high spectrum width and low ρ_{hv}.

3. Simulations of frequency dependence of radar measurements in tornadoes

In this section, radar variable simulations of Z_e and Doppler velocity are presented at multiple frequencies. Relationships between physical properties of the scatterers (e.g., size) and dual-frequency radar variables are also examined.

a. Idealized case study

To illustrate the impact of transmit frequency on Doppler velocity measurements in tornadoes, consider the following simplified example with a 10 000-m^3 resolution volume. In this resolution volume, 100 dry wood plates are simulated with lengths uniformally distributed between 41.6 and 415.7 mm and a thickness of $(1/20)l$, producing a Z_e of 64.5 dBZ at S band using the POA model (Table 3). The maximum S-band equivalent reflectivity factor observed in TDSs is approximately 70 dBZ (e.g., Ryzhkov et al. 2005; Bunkers and Baxter 2011; Bodine et al. 2013), thus suggesting number concentrations are lower than 1 m^{-3} if the debris is assumed to be wood boards (Fig. 3). The resolution volume also contains 3360 0.5-mm- and 85.1 2-mm-diameter drops per cubic meter (assuming the scaling factors used in Table 2), producing an S-band Z_e of 37.6 dBZ. In this example, a simple geometry is assumed such that scatterer motion, wind direction, and the radar beam are aligned. To simulate differences between air and radar-measured wind speeds, the wind speed is 50 m s^{-1}, the wood plate velocity is 40 m s^{-1}, and the 0.5- and 2-mm-diameter drops' velocities are 49 and 47 m s^{-1}, respectively. Slower velocities of the larger scatterers replicate slower tangential velocities of larger scatterers compared to the air velocity. For comparison, Dowell et al. (2005) found that plywood sheet tangential velocities are reduced by about 11 m s^{-1} for their one-dimensional simulation with a vortex radius of 100 m and a maximum tangential velocity of 50 m s^{-1} (see their

Table 2, wind profile 3). In contrast, the raindrops exhibit a smaller tangential velocity reduction of less than $5\,\mathrm{m\,s^{-1}}$.

Simulated Z_e and Doppler velocity for the example resolution volume are shown in Table 3. The term Z_e exhibits large variations across common weather radar frequencies as a consequence of Mie scattering, consistent with Fig. 3. In contrast, raindrops are predominately in the Rayleigh scattering region for centimeter wavelengths, and thus dual-wavelength differences are small. Raindrops are in the Mie scattering region at W band, resulting in lower Z_e.

The large range of dry wood plate Z_e for different frequencies produces an important effect on dominant scatterer type and thus Doppler velocity. At S and C bands, dry wood plate Z_e exceeds raindrop Z_e by at least 10 dB and, consequently, simulated S- and C-band Doppler velocity are within $0.5\,\mathrm{m\,s^{-1}}$ of the wood plates' velocities (Table 3). However, at Ka and W bands, raindrops produce Z_e that exceeds the dry wood plates by 17–20 dB. As a result, the measured Doppler velocities are very close to the velocity of the large drops (which contribute more to Z_e than the small drops in this case). At X band, Z_e contributions from dry wood plates and raindrops are closer; however, the wood plates still have slightly higher Z_e and thus a greater effect on Doppler velocity.

The strong dependence of Doppler velocity on transmit frequency results from the frequency dependence of σ_b. For Rayleigh scatterers,

$$\sigma_b = \frac{\pi^5}{\lambda^4}|K_m|^2 D^6, \tag{9}$$

where $|K_m|$ is a function of the scatterer's refractive index and D is the scatterer's diameter (Doviak and Zrnić 1993). From Eq. (9), it is apparent that σ_b could vary by several orders of magnitude over common weather radar frequencies (e.g., from 3 mm to 10 cm) because of the λ^{-4} dependence. For example, σ_b for a 1-mm-diameter raindrop at S band is $2.84 \times 10^{-6}\,\mathrm{mm^2}$ compared to $1.1\,\mathrm{mm^2}$ at W band. In contrast, σ_b for wood plates exhibits smaller differences among frequencies. For example, σ_b for a 290-mm-length wood board is $2500\,\mathrm{mm^2}$ at S band and $3400\,\mathrm{mm^2}$ at W band. For Rayleigh scatterers, it is apparent that the λ^{-4} dependence in Eq. (9) is removed when Z_e is calculated [Eq. (5)]. However, for scatterers with similar σ_b at different frequencies (e.g., dry or wet wood plates), the λ^4 dependence in Eq. (5) causes much higher Z_e at lower frequencies (longer wavelengths), as illustrated in Fig. 3.

Because raindrop concentrations are several orders of magnitude larger than debris concentration (e.g., $10^3\,\mathrm{m^{-3}}$ compared to $0.01\,\mathrm{m^{-3}}$), frequency differences in σ_b have a significant impact. At W band, σ_b of a wood plate exceeds the 1-mm raindrop by a factor $O(10^3)$ whereas the raindrop concentration exceeds the wood plate concentration by a factor of 10^5. As a result, raindrops are the dominant scatterers when computing Z_e. However, at S band, σ_b of the raindrop is very small, and thus the wood plates dominate the backscattered radar signal. For a similar example with T-matrix calculations, readers are referred to section 3.1 of Bodine et al. (2014a).

TABLE 3. Value of Z_e and mean Doppler velocity for the simplified example with raindrops and debris in a 10 000-$\mathrm{m^3}$ resolution volume. The resolution volume contains 100 dry wood boards with l uniformally distributed between 41.6 and 415.7 mm and a thickness of $(1/20)l$, and 0.5- and 2-mm-diameter raindrops. Term Z_e is computed using the POA model.

Radar frequency band	Wood plates Z_e (dBZ)	Raindrops Z_e (dBZ)	Doppler velocity ($\mathrm{m\,s^{-1}}$)
S	64.5	37.6	40.0
C	51.9	37.4	40.2
X	42.9	37.6	41.6
Ka	18.9	38.6	46.9
W	3.9	20.9	47.7

b. *Multiple frequency simulations of radar variables using LES trajectories*

In this section, concentrations of dry wood boards and raindrops are varied in different experiments to simulate the impact on Z_e, reflectivity-weighted velocity, and dual-frequency radar variables. Simulations are conducted for common weather radar frequencies from S to W bands, and for POA and T-matrix calculations. In the first subsection, a high debris, high raindrop (HDHR) concentration experiment is highlighted for the dry wood board POA calculation. Then, a summary of different experiments is presented for T-matrix experiments and POA calculations for dry and wet wood boards.

Debris and raindrop concentrations vary among tornadoes and even within a single tornado occurrence. Ryzhkov et al. (2005) and Bodine et al. (2013) document the temporal variability of TDSs, indicating variations in debris concentrations or sizes. Spatial distributions and intensities of precipitation vary among supercell thunderstorms, which are often classified as low precipitation (LP), classic, and high precipitation (HP) supercells (e.g., Doswell and Burgess 1993). For supercells with heavier precipitation surrounding the tornado (e.g., classic or HP), greater precipitation entrainment into the tornado may occur. To encompass the expected range of debris and raindrop concentrations in nature, five experiments are performed for a combination of a low, moderate, or high debris concentration scenario (LD, MD, and HD, respectively), and a low, moderate, or high raindrop concentration scenario (LR, MR, and HR, respectively; see Table 2).

For each debris experiment, mean scatterer concentrations are scaled to provide more realistic Z_e based on TDS observations and to maintain stable three-dimensional statistics of scatterer velocities and concentrations. For the HD experiment for dry wood boards, S-band maximum T-matrix Z_e is 62.3 dBZ compared to 67.0 dBZ for the POA model. For the LD and MD experiments, debris concentrations are scaled by a factor of 1/10 and 1/100, respectively, resulting in maximum wood board Z_e of 10 and 20 dB less than the HD experiment, respectively. Finally, it is worth noting that some combinations of debris and rain concentrations produce identical Doppler velocities, DWRs, and dual-frequency velocity differences because the relative contributions of rain and wood boards to Z_e are the same. For example, HDHR and low debris, low raindrop (LDLR) experiments have the same Doppler velocities, DWRs, and dual-frequency velocity differences because the LDLR experiment contains debris and raindrop concentrations that are both scaled by 1/100 from the HDHR experiment. Thus, the experiments producing unique values are presented.

1) HDHR EXPERIMENT

The first experiment simulates a tornado with HDHR concentrations. Simulated Z_e for dry wood boards, raindrops, and all scatterers are shown in Fig. 5 for S, X, and W bands for the POA model. Similar to the idealized example, S-band Z_e is dominated by debris, except where debris concentrations are very small (Figs. 5a–c). At X band, rain and debris are dominant scatterers in different regions of the simulated tornado, resulting in a more complex spatial pattern of Z_e (Figs. 5d–f). Within the volume enclosed by $r < 200$ m and $z < 100$ m, Z_e exhibits larger contributions from debris. In contrast at S and X bands, even large concentrations of debris have little effect on W-band Z_e (Figs. 5g–i), which is evident by very small differences between simulated Z_e for rain and all scatterers.

Since Z_e exhibits greater contributions from debris at S band, S-band reflectivity-weighted velocities deviate significantly from air velocities. For the POA model, radial and tangential reflectivity-weighted scatterer velocities are shown in Figs. 6a,b, and the difference between radial and tangential reflectivity-weighted scatterer velocities and air velocities ($u_{dr} - U$ and $v_{dr} - V$, respectively) are shown in Figs. 6c,d. Comparing u_{dr} and v_{dr} to LES model velocities (Fig. 2), a significant reduction in S-band inflow layer depth and maximum inflow velocities occurs, and tangential velocities are reduced within the radius of maximum wind. The $u_{dr} - U$ exceeds 30 m s^{-1} and occurs where dry wood boards are the dominant scatterers (Fig. 6h). A region of positive $v_{dr} - V$ occurs in the near-surface inflow region (Fig. 6d; $r > 300$ m and $z < 100$ m) where debris with higher tangential velocities falls into a region of relatively low tangential velocity.

At X band, significant differences between air and reflectivity-weighted velocities also occur, but the magnitudes are smaller compared to S band (Fig. 7). Dry wood boards remain the dominant scatterers in the lowest 100–200 m, causing a reduction in maximum inflow velocities. The maximum magnitude of radial velocity errors are 31.7 m s^{-1}, and maximum tangential velocity error is 37.4 m s^{-1} (Figs. 7c,d).

In contrast to the centimeter wavelengths, W-band air and reflectivity-weighted velocities are much smaller (Fig. 8). W-band u_{dr} and v_{dr} exhibit close agreement to model wind fields, and the depth and peak inflow velocities are well resolved. The dominant scatterers are raindrops, resulting in smaller magnitudes of $u_{dr} - U$ and $v_{dr} - V$, generally less than 10 m s^{-1}. Some large positive tangential velocity errors occur near the tornado's central axis near the surface. Since raindrops acquire substantial negative radial velocities in the inflow region, they continue moving toward the central axis of the tornado. These drops acquire higher tangential velocities near the radius of maximum wind, and they continue moving radially inward where tangential velocities are lower, producing positive $v_{dr} - V$. Overall, W-band velocity measurements are generally shown to be more robust to debris centrifuging errors even in a case with the highest expected debris concentrations in TDSs (e.g., S-band Z_e approaching 70 dBZ).

Dual-frequency measurements may provide information about the spatial structure and magnitudes of velocity bias, and dominant scatterer size. Since the S- and W-band radars are sensitive to different scatterer sizes, dual-frequency velocity differences between radial and tangential reflectivity-weighted velocities (S–W DDU and S–W DDV, respectively) exhibit large differences (Figs. 6e,f). The spatial structure of S–W DDU exhibits good correlation S-band $u_{dr} - U$ with a correlation coefficient of 0.98 (Table 6), and DDU has an RMSE of 2.4 m s^{-1} as an estimator of $u_{dr} - U$. DDV also exhibits good correlation with S-band $v_{dr} - V$ with a correlation coefficient of 0.88 and an RMSE of 2.9 m s^{-1}. DWRs may also provide useful information about debris size. S–W-band DWRs and dominant scatterer radius are shown in Figs. 6g,h. S–W-band DWRs exhibit good correlation (0.87) with dominant scatterer radius (Table 6). Using a DWR between S and X bands, the correlation with debris size is 0.88. Using reflectivity measurements at X band would avoid significant attenuation issues for estimating DWRs at W band.

X–W-band DDU exhibits high correlation with X-band $u_{dr} - U$, with a correlation coefficient of 0.95,

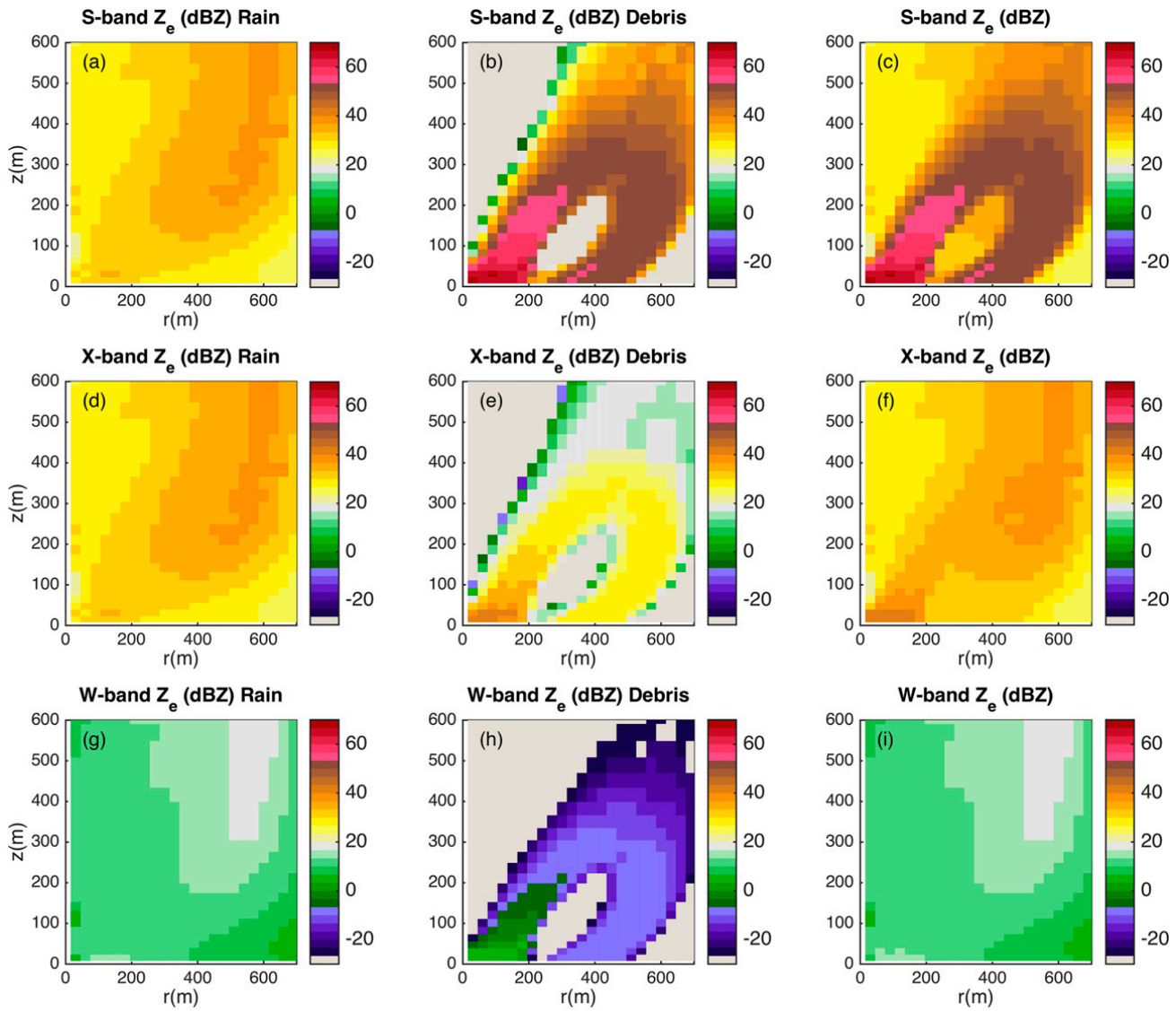

FIG. 5. Term Z_e (dBZ) for rain, debris, and all scatterers at (a)–(c) S band, (d)–(f) X band, and (g)–(i) W band for the HDHR concentration experiment and POA model for dry wood boards. The Z_e contributions of rain and debris to total Z_e vary substantially depending on radar frequency. At lower (higher) frequencies, debris (rain) is the dominant contributor to total Z_e, while at intermediate frequencies (X band) total Z_e has substantial contributions from both rain and debris.

and X–W-band DDV exhibits a weaker correlation coefficient of 0.75 with X-band $v_{dr} - V$ (Table 6). Dual-frequency velocity differences poorly estimate $v_{dr} - V$ where raindrops are dominant scatterers (i.e., DWRs are smaller), and thus the impact of excluding such regions is examined. The correlation coefficient between X–W-band DDV and X-band $v_{dr} - V$ where DWRs exceed 15 dB (i.e., debris are dominant scatterers) is 0.86.

2) SUMMARY OF EXPERIMENTS

The mean $u_{dr} - U$ within the lowest 300 m for the five experiments is computed for the POA model for dry and wet wood boards (Table 4), and T-matrix electromagnetic models for dry wood boards (Table 5). From left to right, the relative Z_e contributions of rain increase; and in the HDLR (LDHR) experiment, debris (rain) has its maximum relative contributions to Z_e. As the contribution by rain increases, the mean $u_{dr} - U$ decreases. At Ka and W bands, the mean errors are less than $4\,\mathrm{m\,s^{-1}}$ for all experiments except HDLR. Thus, for the experiment with the highest debris concentration and lowest raindrop concentration experiment, large debris may become the dominant scatterer at millimeter wavelengths. However, millimeter-wavelength T-matrix mean $u_{dr} - U$ is lower than the POA model because Z_e is lower. In contrast to millimeter wavelengths, the mean errors at S and C bands frequently exceed $10\,\mathrm{m\,s^{-1}}$. The X band exhibits the greatest sensitivity to the relative contributions of debris and rain, with

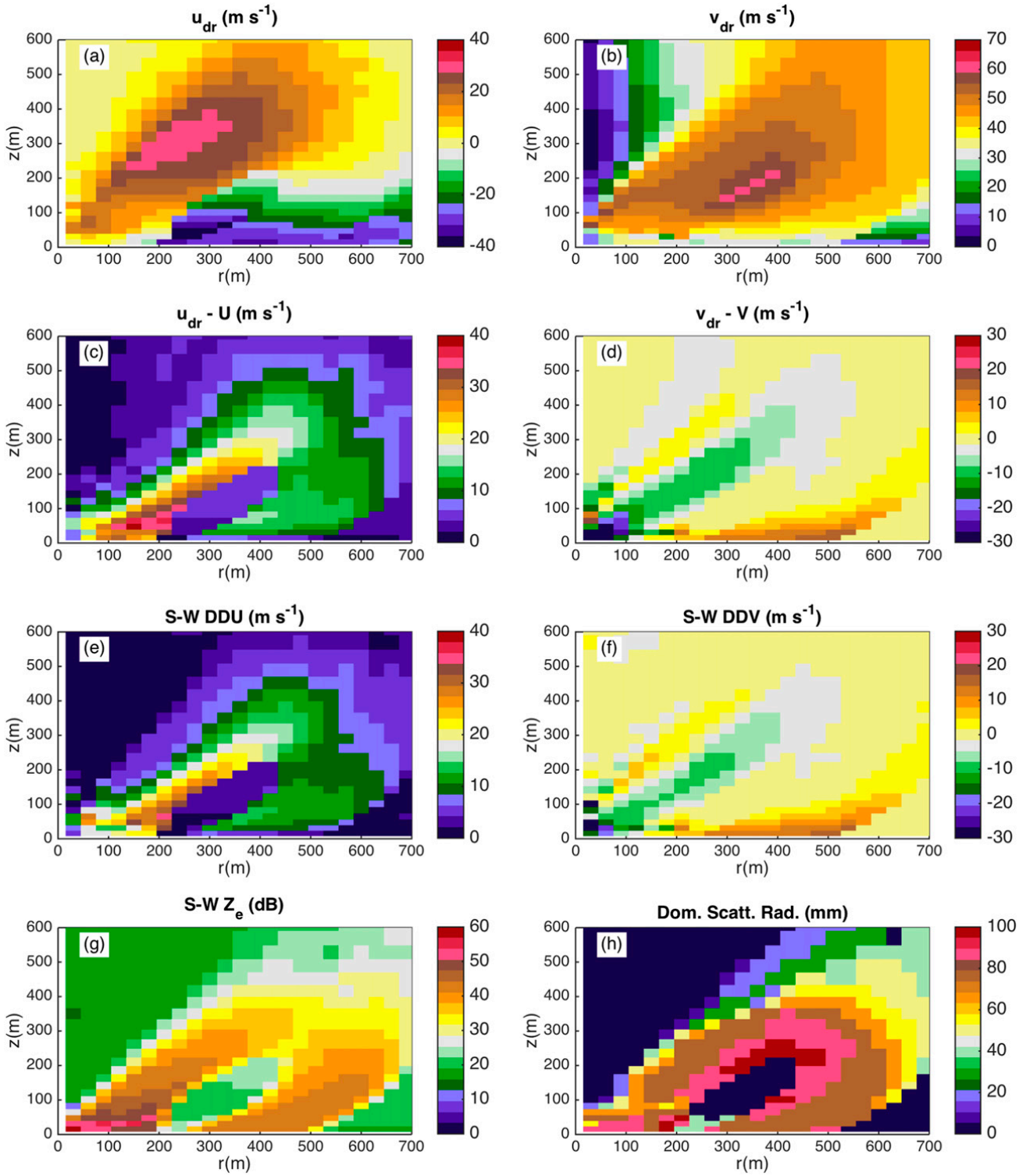

FIG. 6. S-band (a) u_{dr} and (b) v_{dr}, S-band (c) $u_{dr} - U$ and (d) $v_{dr} - V$, S–W (e) DDU and (f) DDV, (g) S–W Z_e difference, and (h) S-band dominant scatterer radius for the HDHR experiment and POA model for dry wood boards. Positive u_{dr} occurs within the inflow layer, producing high $u_{dr} - U$ exceeding 30 m s^{-1}. Dual-frequency velocity differences, S–W DDU and S–W DDV, exhibit similar spatial structure and magnitudes as differences between air and simulated Doppler velocities ($u_{dr} - U$ and $v_{dr} - V$, respectively).

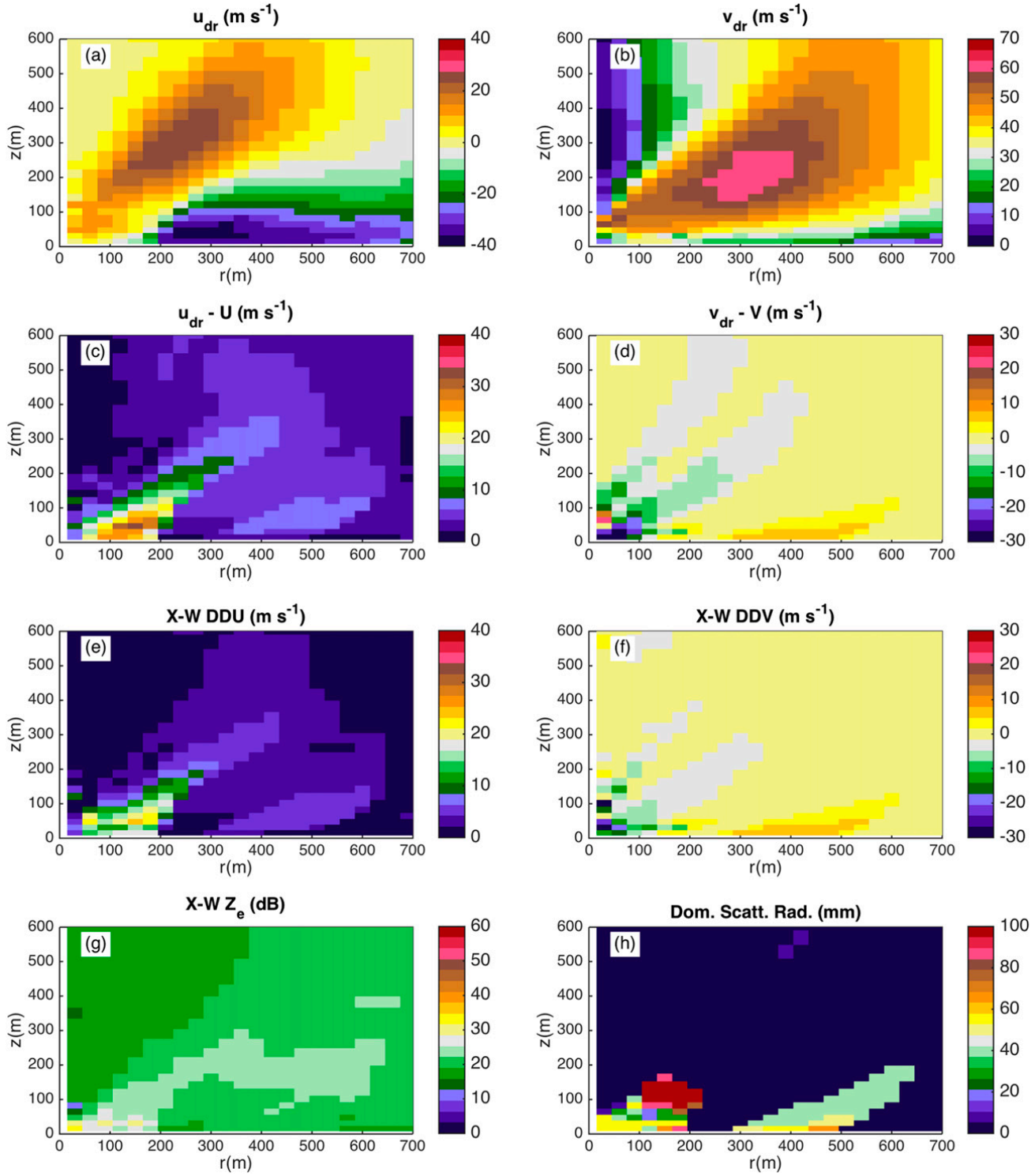

FIG. 7. X-band (a) u_{dr} and (b) v_{dr}, X-band (c) $u_{dr} - U$ and (d) $v_{dr} - V$, X–W (e) DDU and (f) DDV, (g) X–W Z_e difference, and (h) X-band dominant scatterer radius for the HDHR experiment and POA model for dry wood boards. Similar to X band, positive u_{dr} occurs in the inflow layer, resulting in X-band $u_{dr} - U$ exceeding $20\,\mathrm{m\,s^{-1}}$.

mean errors of $11.2\,\mathrm{m\,s^{-1}}$ for the HDLR experiment compared to $4.2\,\mathrm{m\,s^{-1}}$ for the LDHR experiment.

DWRs exhibit strong correlations with debris size when debris is the dominant scatterers. For the dry wood board experiments, correlation coefficients between DWR and scatterer size are shown for the two electromagnetic models and different frequency pairs in Tables 6 and 7. Correlation coefficients exceed 0.87 for the high debris

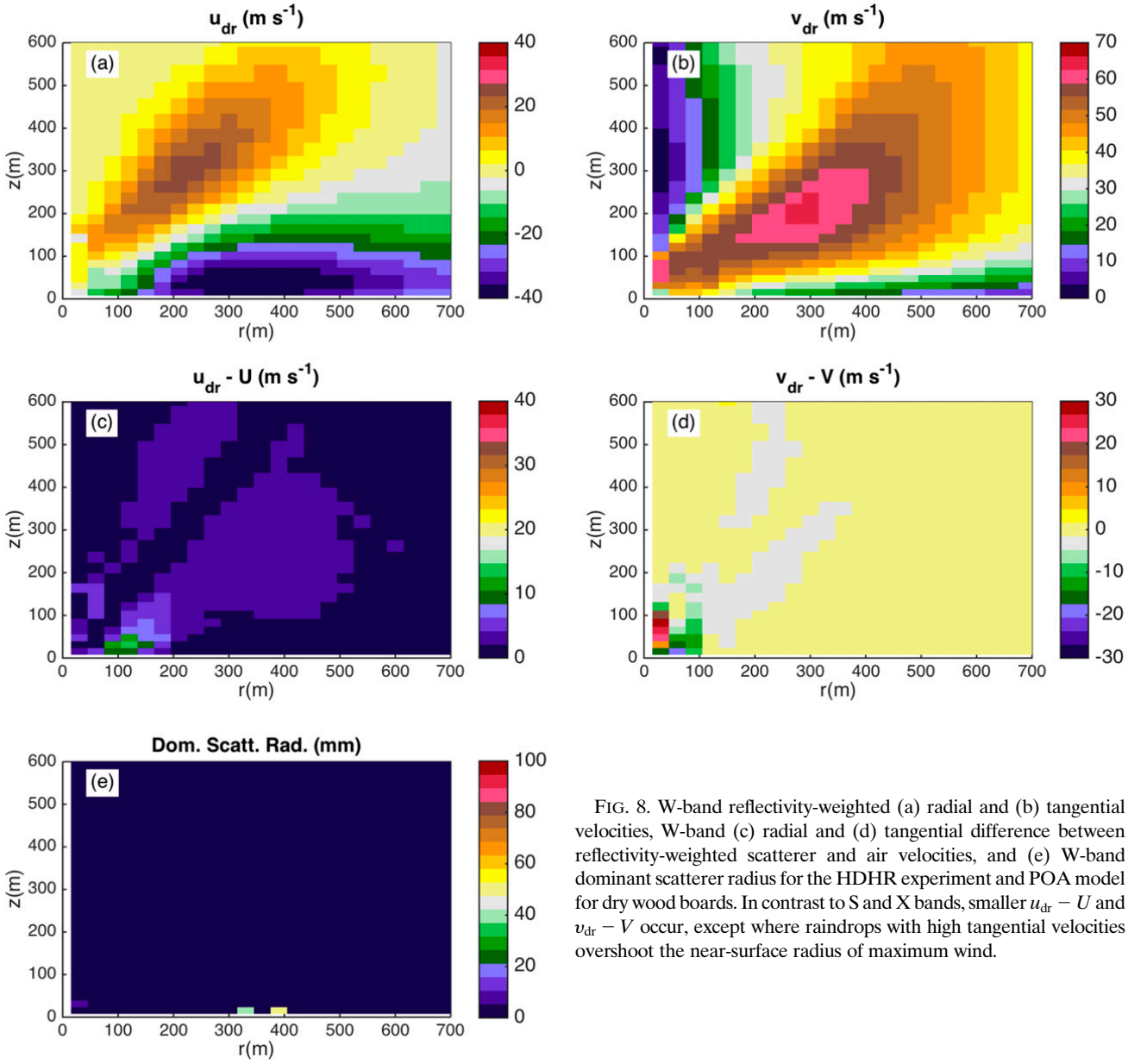

FIG. 8. W-band reflectivity-weighted (a) radial and (b) tangential velocities, W-band (c) radial and (d) tangential difference between reflectivity-weighted scatterer and air velocities, and (e) W-band dominant scatterer radius for the HDHR experiment and POA model for dry wood boards. In contrast to S and X bands, smaller $u_{dr} - U$ and $v_{dr} - V$ occur, except where raindrops with high tangential velocities overshoot the near-surface radius of maximum wind.

experiments for the POA model. Because W-band attenuation can be significant, the S–X DWR would be the most practical and it exhibits the highest overall correlation with scatterer size. For the X–W DWR, correlation coefficients are low for the heavy rain experiments because Rayleigh scatterers become dominant and DWRs decrease.

At present, no method exists to measure differences in air and Doppler velocities in tornadoes using radar observations. Dual-frequency velocity differences [Eqs. (7) and (8)] exhibit strong correlation in some cases, which could enable estimates of differences between air and radar-measured velocity. Correlation coefficients between DDU and $u_{dr} - U$, and DDV and $v_{dr} - V$, are shown in Tables 6 and 7. S–W and X–W DDU and S- and X-band $u_{dr} - U$ exhibit high correlation for the three middle POA model experiments (HDMR, HDHR, and MDHR). The highest correlation occurs when debris (raindrops) is the dominant scatterer at the lower (higher) frequency. Accordingly, correlation coefficients are generally lower for the HDLR (LDHR) experiments because debris (raindrops) exhibits a large contribution to velocity at both frequencies.

For wet wood boards in the POA model compared to dry wood boards, the primary difference is that Z_e increases for debris and results in higher values of mean $u_{dr} - U$ (Table 4). The primary trends, however, remain similar to the dry case with mean $u_{dr} - U$ still decreasing as the contribution of rain increases (i.e., from left to right) and X

TABLE 4. RMSEs for POA model RCS-simulated mean radial velocity error ($u_{dr} - U$; m s^{-1}) in the lowest 300 m at S, C, X, Ka, and W bands for the five experiments with contributions of raindrops (wood boards) increasing (decreasing) from left to right. Mean errors are shown for both dry and wet debris calculations.

Experiment	HDLR	HDMR	HDHR	MDHR	LDHR
S band (dry)	11.8	11.7	11.5	10.9	8.9
C band (dry)	11.0	10.5	9.2	6.6	4.6
X band (dry)	11.2	10.0	7.3	4.9	4.2
Ka band (dry)	6.3	3.6	3.1	3.0	3.0
W band (dry)	7.4	3.9	2.3	2.0	2.0
S band (wet)	11.6	11.5	11.4	11.0	9.6
C band (wet)	11.8	11.7	11.2	9.4	6.4
X band (wet)	11.5	11.0	6.1	6.1	4.5
Ka band (wet)	8.4	5.2	3.4	3.0	3.0
W band (wet)	9.4	6.2	3.2	2.2	2.0

band exhibiting the largest range of $u_{dr} - U$. It is stressed that the raindrop concentration did not change from the dry to wet debris case. So, this comparison reflects a scenario in which the moisture content of the wet board changes, but the background precipitation does not change.

c. *Frequency dependence of vertical wind retrievals*

Vertical velocities in tornadoes are often obtained using the GBVTD from retrieved radial winds (e.g., Lee and Wurman 2005; Kosiba and Wurman 2010; Wakimoto et al. 2012). To examine how debris centrifuging errors impact vertical velocity retrievals at different frequencies, vertical velocities are obtained by integrating the Boussinesq form of the continuity equation using simulated u_{dr} for different experiments. Retrieved S-, X-, and W-band vertical velocities are shown in Figs. 9a–c for the HDHR experiment with dry wood boards and the POA model. As illustrated by Nolan (2013), debris centrifuging effects increase downdraft velocities; however, these vertical velocity errors depend on the dominant scatterer type and frequency. For the HDHR experiment, S-band retrievals produce an anomalously strong downdraft, whereas W-band vertical velocity errors are smaller. At S and X bands, a two-cell vortex results (i.e., downdraft reaches the surface), whereas the W-band retrieval produces a vortex breakdown flow consistent with model vertical velocities. Moreover, updraft intensity is increased at S and X bands as a consequence of near-surface anomalous retrieved convergence generated by radial gradients of large debris and u_{dr} at a radius of 200 m (Figs. 5–7).

TABLE 6. Correlation coefficients for the dry wood board simulations using the POA model, including DWR and scatterer size, DDU and $u_{dr} - U$, and DDV and $v_{dr} - V$. Correlation coefficients are computed for S–W and X–W bands, and for S–X DWR.

Experiment	HDLR	HDMR	HDHR	MDHR	LDHR
S–W Z_e	0.93	0.91	0.87	0.81	0.64
S–X Z_e	0.95	0.94	0.88	0.80	0.70
X–W Z_e	0.88	0.80	0.47	0.11	−0.07
S–W DDU	0.58	0.90	0.98	0.98	0.97
S–W DDV	0.66	0.81	0.88	0.88	0.84
X–W DDU	0.55	0.89	0.95	0.82	0.58
X–W DDV	0.57	0.74	0.75	0.56	0.38

To assess the effectiveness of the debris centrifuging correction proposed by Wakimoto et al. (2012), the radial velocity bias of 0.5-, 1.5-, and 4-mm-diameter drops is subtracted from simulated u_{dr}, and then vertical velocities are recomputed. The RMSEs for S, X, and W bands for uncorrected and corrected vertical velocity retrievals are shown in Table 8, and corrected vertical velocities are shown for the HDHR experiment for 4-mm-diameter drops (Fig. 9d,e). For S- and X-band corrected vertical velocities, a vortex breakdown flow is obtained after correction, and downdraft velocities are reduced. For all S-band experiments, the correction reduces RMSEs for all drop sizes, although RMSEs still exceed 10 m s^{-1}. At X band, the correction generally reduces RMSEs. For the LDHR experiment, RMSEs increase for the 4-mm-diameter correction and thus estimating drop size may be important. For the HDHR and HDLR experiments, RMSEs exceed 10 m s^{-1} even

TABLE 5. RMSEs for T-matrix-simulated mean radial velocity error ($u_{dr} - U$; m s^{-1}) in the lowest 300 m at S, C, X, Ka, and W bands for the four experiments with contributions of raindrops (dry wood boards) increasing (decreasing) from left to right. In contrast to the POA model, lower mean radial velocity errors are observed at millimeter wavelengths.

Experiment	HDLR	HDMR	HDHR	MDHR	LDHR
S band	11.6	11.6	11.3	10.2	7.5
C band	11.4	11.0	9.6	6.8	4.7
X band	10.6	8.9	6.1	4.5	4.1
Ka band	5.1	3.3	3.0	3.0	3.0
W band	2.3	2.0	2.0	2.0	2.0

TABLE 7. Correlation coefficients for the dry wood board simulations using T-matrix calculations, including dual-frequency Z_e differences and scatterer size, DDU and $u_{dr} - U$, and DDV and $v_{dr} - V$. Correlation coefficients are computed for S–W and X–W bands.

Experiment	HDLR	HDMR	HDHR	MDHR	LDHR
S–W Z_e	0.89	0.87	0.84	0.74	0.48
S–X Z_e	0.90	0.88	0.83	0.72	0.69
X–W Z_e	0.75	0.65	0.33	0.03	−0.07
S–W DDU	0.98	0.98	0.98	0.98	0.96
S–W DDV	0.90	0.89	0.88	0.86	0.79
X–W DDU	0.98	0.97	0.92	0.69	0.54
X–W DDV	0.87	0.83	0.70	0.43	0.39

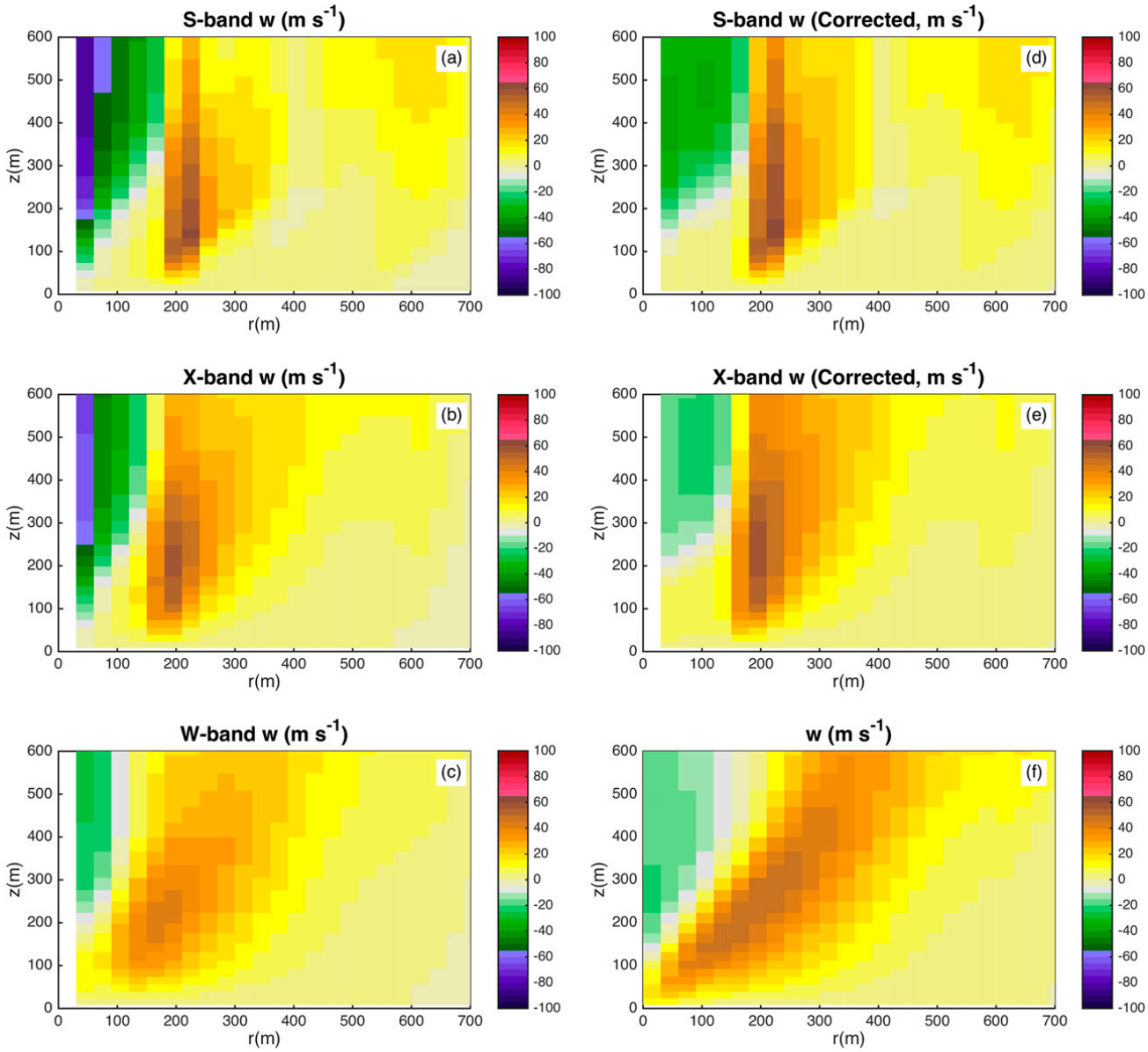

FIG. 9. Retrieved (a) S-, (b) X-, and (c) W-band vertical velocities ($\mathrm{m\,s^{-1}}$) for the HDHR experiment and POA model for dry wood boards without debris centrifuging correction. (d),(e) As in (a),(b), but with debris centrifuging correction for 4-mm diameter drops. (f) Term w ($\mathrm{m\,s^{-1}}$) on the same axisymmetric grid. Anomalously strong downdrafts and two-cell vortex flow are produced at S and X bands. However, more realistic vertical velocities are obtained after debris centrifuging correction.

with a correction for a 4-mm-diameter drop. At W band, corrections for the LDHR and HDHR experiments adversely affect retrievals unless the smallest drop size is used (Table 8). W-band RMSEs exceed $10\,\mathrm{m\,s^{-1}}$ for the HDLR experiment even though the correction is applied.

4. Conclusions

Radar variable simulations are conducted with an LES model, scatterer trajectories, and electromagnetic scattering calculations to examine the frequency dependence of Z_e and Doppler velocity in tornadoes. Simulations are conducted using a range of raindrop and wood board sizes and concentrations to represent typical small and large scatterers in tornadoes. The simulations reveal the significant frequency dependence of Z_e and Doppler velocity. A strong frequency dependence of σ_b for small scatterers results in significant changes in dominant scatterer types from S to W band. At S (W) band, dominant scatterers are wood boards (rain), except when their concentrations are very low. As a result, air and simulated Doppler velocities exhibit decreasing mean differences as the radar frequency

TABLE 8. Simulated retrieved vertical velocity RMSEs at S, X, and W bands for the LDHR, HDHR, and HDLR experiments, and POA model for dry wood boards. RMSEs for uncorrected and corrected vertical velocity retrievals are presented, and are calculated within a radius of 300 m (i.e., where the largest vertical velocity errors are present). In parentheses, drop diameters used for correction are listed, and NC is listed for cases with no correction applied.

Experiment	S band	X band	W band
LDHR (NC)	17.0	8.1	7.3
LDHR (0.5 mm)	15.4	7.4	7.4
LDHR (1.5 mm)	13.6	7.8	9.0
LDHR (4 mm)	12.3	9.4	11.4
HDHR (NC)	20.7	14.8	7.5
HDHR (0.5 mm)	19.1	13.2	7.3
HDHR (1.5 mm)	17.1	11.4	8.4
HDHR (4 mm)	15.1	10.9	10.7
HDLR (NC)	21.4	20.6	16.0
HDLR (0.5 mm)	19.8	18.9	14.6
HDLR (1.5 mm)	17.5	16.8	13.1
HDLR (4 mm)	15.5	14.8	12.1

increases. At intermediate frequencies (e.g., X band), the dominant scatterer type and air and simulated Doppler velocity differences exhibit large variability depending on the relative concentrations of raindrops and wood boards. Finally, higher Z_e is observed at each frequency for wet wood boards compared to dry wood boards, resulting in greater mean velocity differences.

Dual-frequency variables for estimating air and Doppler velocity differences and scatterer size are explored. For the middle three POA experiments, high correlations are found between the radial dual-frequency velocity differences (DDU) and the differences between radial air and simulated Doppler velocities. For the HDLR and LDHR experiments, correlations are reduced because the dominant scatterer type is the same at both frequencies (i.e., debris for HDLR and rain for LDHR). When high concentrations of debris are present, DWRs exhibit high correlation with debris size, particularly for S–X-band DWRs. Finally, DWRs were examined for both dry and wet wood boards, and DWR changes (< 2 dB) were smaller than the increase in Z_e.

These simulations reveal that diagnosing the dominant scatterer type in tornadoes is a complex process and that the frequency dependence of electromagnetic scattering must be considered. The highest sensitivity to relative contributions of rain and debris occurs at X band, which is a commonly used frequency for mobile radar observations of tornadoes. Thus, dual-frequency or polarimetric radar observations are needed at X band to justify assumptions about dominant scatterer type (e.g., using DWRs or ρ_{hv}). Moreover, significant residual errors often remain at S and X bands even after debris centrifuging corrections for raindrops are applied. Thus, for cases where raindrops or Rayleigh scatterers are not the dominant scatterers, additional methods are needed to correct air and Doppler velocity differences. Such corrections are important, as tornadoes with higher enhanced Fujita scale ratings typically have high Z_e (e.g., Bunkers and Baxter 2011; Schultz et al. 2012b; Bodine et al. 2013) and likely greater concentrations of lofted debris.

As demonstrated in section 3, dual-frequency velocity differences and DWRs have the potential to estimate scatterer-induced velocity bias and scatterer sizes. Dual-frequency spectral analysis could help distinguish Rayleigh and non-Rayleigh scatterers, and perhaps aid in correcting scatterer-induced velocity bias by identifying velocities of smaller scatterers. To develop corrections for single-frequency polarimetric radars, comparisons between dual-frequency velocity data and polarimetric radar variables may enable robust corrections for velocity errors at single frequencies. Dual-polarization variables such as ρ_{hv} and differential velocity (Snyder and Bluestein 2014) may exhibit relationships to debris characteristics, in addition to polarimetric spectral densities. Photogrammetry and video observations could also aid in determining how well polarimetric and dual-frequency observations characterize debris size and differences between air and Doppler velocities.

It is emphasized that the results presented in this study are based on simulations, and thus observational validation of the frequency dependence of radar variables is needed. An optimal platform for examining the frequency dependence would be a mobile dual-frequency radar with a matched antenna pattern. Until such systems are developed, collocated mobile radars operating at different frequencies could be used to investigate the frequency dependence if temporal and spatial sampling differences are minimized (e.g., coordinated scans, matched pulse lengths). Dual-frequency capability for fixed radars could also provide opportunities to examine the frequency dependence of radar observations because multiple high-impact tornado events have occurred in proximity to fixed radars (e.g., Ryzhkov et al. 2005; Palmer et al. 2011; Schultz et al. 2012a,b; Atkins et al. 2014; Kurdzo et al. 2015).

Because only one debris type is examined herein, future studies are planned to obtain RCSs of a large set of tornado debris types using laboratory measurements and advanced electromagnetic simulations. These studies will encompass natural debris (e.g., leaves, tree branches, soils) and anthropogenic debris (e.g., wood boards, insulation), and examine more realistic scatterer shapes (2 in. × 4 in. lumber, or rectangular wood sheathing). These efforts include RCSs computed using Ansys high-frequency simulation software (HFSS) and RCS measurements in anechoic chambers at the Advanced Radar Research Center at the University of Oklahoma. Using the RCS

data, polarimetric TDSs are simulated using a polarimetric radar time series simulator (Cheong et al. 2015) that ingests wind data from high-resolution models (e.g., LES model herein). Using the radar simulator, polarimetric and dual-frequency radar signatures of different scatterer types can be explored, and new methods to characterize debris size and correct debris centrifuging errors can be developed and tested. Such efforts are critical to advancing scientific understanding of tornado dynamics and improving radar estimates of wind speeds used to assess enhanced Fujita scale ratings.

Acknowledgments. This study is based upon work supported by the National Science Foundation under Grants. AGS-1303685 and OISE-1209444. The first author is supported by the National Center for Atmospheric Research (NCAR) Advanced Study Program. This study emerged from a substantial collaborative effort between the University of Oklahoma and the Disaster Prevention Research Institute (DPRI) at Kyoto University, and the first author is grateful to Prof. Maruyama and Kyoto University for hosting his stay. The authors would also like to acknowledge the Collaborative Research program of the Joint Usage/Collaborative Research Center for Multidisciplinary Disaster Prevention Study: DPRI Kyoto University. The authors thank Scott Ellis, Wen-Chau Lee, and Tammy Weckwerth for reviewing an early version of the manuscript. Four anonymous reviewers also provided excellent feedback, which improved the clarity of the discussions.

REFERENCES

Atkins, N. T., K. M. Butler, K. R. Flynn, and R. M. Wakimoto, 2014: An integrated damage, visual, and radar analysis of the 2013 Moore Oklahoma EF5 tornado. *Bull. Amer. Meteor. Soc.*, **95**, 1549–1561, doi:10.1175/BAMS-D-14-00033.1.

Atlas, D., 1953: Scattering and attenuation by non-spherical atmospheric particles. *J. Atmos. Terr. Phys.*, **3**, 108–119, doi:10.1016/0021-9169(53)90093-2.

——, and F. H. Ludlam, 1961: Multi-wavelength radar reflectivity of hailstorms. *Quart. J. Roy. Meteor. Soc.*, **87**, 523–534, doi:10.1002/qj.49708737407.

Balanis, C. A., 2012: *Advanced Engineering Electromagnetics*. 2nd ed. John Wiley & Sons, 1018 pp.

Bluestein, H. B., M. M. French, R. L. Tanamachi, S. Frasier, K. Hardwick, F. Junyent, and A. Pazmany, 2007: Close-range observations of tornadoes in supercells made with a dual-polarization, X-band, mobile Doppler radar. *Mon. Wea. Rev.*, **135**, 1522–1543, doi:10.1175/MWR3349.1.

Bodine, D. J., 2014: Polarimetric radar observations and numerical simulations of tornadic debris. Ph.D. dissertation, University of Oklahoma, 264 pp.

——, M. R. Kumjian, R. D. Palmer, P. L. Heinselman, and A. V. Ryzhkov, 2013: Tornado damage estimation using polarimetric radar. *Wea. Forecasting*, **28**, 139–158, doi:10.1175/WAF-D-11-00158.1.

——, R. D. Palmer, T. Maruyama, C. J. Fulton, and B. L. Cheong, 2014a: Dual-frequency simulations of radar observations of tornadoes. *27th Conf. on Severe Local Storms*, Madison, WI, Amer. Meteor. Soc., 15A.2. [Available online at https://ams.confex.com/ams/27SLS/webprogram/Paper254253.html.]

——, ——, and G. Zhang, 2014b: Dual-wavelength polarimetric radar analyses of tornadic debris signatures. *J. Appl. Meteor. Climatol.*, **53**, 242–261, doi:10.1175/JAMC-D-13-0189.1.

Bunkers, M. J., and M. A. Baxter, 2011: Radar tornadic debris signatures on 27 April 2011. *Electron. J. Oper. Meteor.*, **12** (7). [Available online at http://www.nwas.org/ej/2011-ION1/index.html.]

Cheong, B. L., R. D. Palmer, and M. Xue, 2008: A time series weather radar simulator based on high-resolution atmospheric models. *J. Atmos. Oceanic Technol.*, **25**, 230–243, doi:10.1175/2007JTECHA923.1.

——, D. Bodine, Y. Zhu, C. Fulton, S. Torres, T. Maruyama, and R. Palmer, 2015: Emulating polarimetric radar signals from tornadic debris using a radar-cross-section library. *European Radar Conference (EuRAD)*, Paris, France, IEEE, 249–252, doi:10.1109/EuRAD.2015.7346284.

Church, C. R., J. T. Snow, G. L. Baker, and E. M. Agee, 1979: Characteristics of tornado-like vortices as a function of swirl ratio: A laboratory investigation. *J. Atmos. Sci.*, **36**, 1755–1776, doi:10.1175/1520-0469(1979)036<1755:COTLVA>2.0.CO;2.

Daian, G., A. Taube, A. Birnboim, M. Daian, and Y. Shramkov, 2006: Modeling the dielectric properties of wood. *Wood Sci. Technol.*, **40**, 237–246, doi:10.1007/s00226-005-0060-7.

Davies-Jones, R. P., 1973: The dependence of core radius on swirl ratio in a tornado simulator. *J. Atmos. Sci.*, **30**, 1427–1430, doi:10.1175/1520-0469(1973)030<1427:TDOCRO>2.0.CO;2.

Doswell, C. A., III, and D. W. Burgess, 1993: Tornadoes and tornadic storms: A review of conceptual models. *The Tornado: Its Structure, Dynamics, Prediction and Hazards, Geophys. Monogr.*, Vol. 79, Amer. Geophys. Union, 161–172, doi:10.1029/GM079p0161.

Doviak, R. J., and D. S. Zrnić, 1993: *Doppler Radar and Weather Observations*. 2nd ed. Dover Publications, 562 pp.

Dowell, D. C., C. R. Alexander, J. M. Wurman, and L. J. Wicker, 2005: Centrifuging of hydrometeors and debris in tornadoes: Radar-reflectivity patterns and wind-measurement errors. *Mon. Wea. Rev.*, **133**, 1501–1524, doi:10.1175/MWR2934.1.

Holmes, J. D., C. J. Baker, and Y. Tamura, 2006: Tachikawa number: A proposal. *J. Wind Eng. Ind. Aerodyn.*, **94**, 41–47, doi:10.1016/j.jweia.2005.10.004.

Jebbor, N., S. Bri, A. Nakheli, L. Bejjit, M. Hdddad, and A. Mamouni, 2011: Complex permittivity determination with the transmission/reflection method. *Int. J. Emerg. Sci.*, **4**, 682–695.

Knott, E. F., M. T. Tuley, and J. F. Shaeffer, 1993: *Radar Cross Section*. 2nd ed. Artech House, 611 pp.

Kosiba, K., and J. Wurman, 2010: The three-dimensional axisymmetric wind field structure of the Spencer, South Dakota, 1998 tornado. *J. Atmos. Sci.*, **67**, 3074–3083, doi:10.1175/2010JAS3416.1.

Kumjian, M. R., and A. V. Ryzhkov, 2008: Polarimetric signatures in supercell thunderstorms. *J. Appl. Meteor. Climatol.*, **47**, 1940–1961, doi:10.1175/2007JAMC1874.1.

Kurdzo, J. M., D. J. Bodine, B. L. Cheong, and R. D. Palmer, 2015: High-temporal resolution polarimetric X-band Doppler radar observations of the 20 May 2013 Moore, Oklahoma tornado. *Mon. Wea. Rev.*, **143**, 2711–2735, doi:10.1175/MWR-D-14-00357.1.

Lee, W.-C., and J. Wurman, 2005: Diagnosed three-dimensional axisymmetric structure of the Mulhall tornado on 3 May 1999. *J. Atmos. Sci.*, **62**, 2373–2393, doi:10.1175/JAS3489.1.

——, B. J.-D. Jou, P.-L. Chang, and S.-M. Deng, 1999: Tropical cyclone kinematic structure retrieved from single-Doppler radar observations. Part I: Doppler velocity patterns and the GBVTD technique. *Mon. Wea. Rev.*, **127**, 2419–2439, doi:10.1175/1520-0493(1999)127<2419:TCKSRF>2.0.CO;2.

Lewellen, D. C., B. Gong, and W. S. Lewellen, 2008: Effects of finescale debris on near-surface tornado dynamics. *J. Atmos. Sci.*, **65**, 3247–3262, doi:10.1175/2008JAS2686.1.

Marshall, J. S., and W. M. K. Palmer, 1948: The distribution of raindrops with size. *J. Meteor.*, **5**, 165–166, doi:10.1175/1520-0469(1948)005<0165:TDORWS>2.0.CO;2.

Maruyama, T., 2011: Simulation of flying debris using a numerically generated tornado-like vortex. *J. Wind Eng. Ind. Aerodyn.*, **99**, 249–256, doi:10.1016/j.jweia.2011.01.016.

Matrosov, S. Y., 2011: Feasibility of using radar differential Doppler velocity and dual-frequency ratio for sizing particles in thick ice clouds. *J. Geophys. Res.*, **116**, D17202, doi:10.1029/2011JD015857.

McDonald, J. R., G. S. Forbes, and T. P. Marshall, 2004: The enhanced Fujita (EF) scale. *22nd Conf. on Severe Local Storms*, Hyannis, MA, Amer. Meteor. Soc., 3B.2. [Available online at https://ams.confex.com/ams/11aram22sls/techprogram/paper_81090.htm.]

Mishchenko, M. I., 2000: Calculation of the amplitude matrix for a nonspherical particle in a fixed orientation. *Appl. Opt.*, **39**, 1026–1031, doi:10.1364/AO.39.001026.

——, L. D. Travis, and D. W. Mackowski, 1996: T-matrix computations of light scattering by nonspherical particles: A review. *J. Quant. Spectrosc. Radiat. Transfer*, **55**, 535–575, doi:10.1016/0022-4073(96)00002-7.

Nolan, D. S., 2013: On the use of Doppler radar–derived wind fields to diagnose the secondary circulations of tornadoes. *J. Atmos. Sci.*, **70**, 1160–1171, doi:10.1175/JAS-D-12-0200.1.

Palmer, R. D., and Coauthors, 2011: The 10 May 2010 tornado outbreak in central Oklahoma: Potential for new science with high-resolution polarimetric radar. *Bull. Amer. Meteor. Soc.*, **92**, 871–891, doi:10.1175/2011BAMS3125.1.

Picca, J., and A. Ryzhkov, 2012: A dual-wavelength polarimetric analysis of the 16 May 2010 Oklahoma City extreme hailstorm. *Mon. Wea. Rev.*, **140**, 1385–1403, doi:10.1175/MWR-D-11-00112.1.

Ray, P. S., 1972: Broadband complex refractive indices of ice and water. *Appl. Opt.*, **11**, 1836–1844, doi:10.1364/AO.11.001836.

Ryzhkov, A. V., T. J. Schuur, D. W. Burgess, and D. S. Zrnić, 2005: Polarimetric tornado detection. *J. Appl. Meteor.*, **44**, 557–570, doi:10.1175/JAM2235.1.

Schultz, C. J., and Coauthors, 2012a: Dual-polarization tornadic debris signatures Part I: Examples and utility in an operational setting. *Electron. J. Operational Meteor.*, **13**, 120–137.

——, and Coauthors, 2012b: Dual-polarization tornadic debris signatures Part II: Comparisons and caveats. *Electron. J. Operational Meteor.*, **13**, 138–150.

Senior, T. B., K. Sarabandi, and F. T. Ulaby, 1987: Measuring and modeling the backscattering cross section of a leaf. *Radio Sci.*, **22**, 1109–1116, doi:10.1029/RS022i006p01109.

Simiu, E., and R. H. Scanlan, 1996: *Wind Effects on Structures: Fundamentals and Applications to Design*. 3rd ed. John Wiley, 688 pp.

Snow, J. T., 1984: On the formation of particle sheaths in columnar vortices. *J. Atmos. Sci.*, **41**, 2477–2491, doi:10.1175/1520-0469(1984)041<2477:OTFOPS>2.0.CO;2.

——, A. L. Wyatt, A. K. McCarthy, and E. K. Bishop, 1995: Fallout of debris from tornadic thunderstorms: A historical perspective and two examples from VORTEX. *Bull. Amer. Meteor. Soc.*, **76**, 1777–1790, doi:10.1175/1520-0477(1995)076<1777:FODFTT>2.0.CO;2.

Snyder, J. C., and H. B. Bluestein, 2014: Some considerations for the use of high-resolution mobile radar data in tornado intensity determination. *Wea. Forecasting*, **29**, 799–827, doi:10.1175/WAF-D-14-00026.1.

——, ——, G. Zhang, and S. J. Frasier, 2010: Attenuation correction and hydrometeor classification of high-resolution, X-band, dual-polarized mobile radar measurements in severe convective storms. *J. Atmos. Oceanic Technol.*, **27**, 1979–2001, doi:10.1175/2010JTECHA1356.1.

Uchida, T., and Y. Ohya, 2003: Large-eddy simulation of turbulent airflow over complex terrain. *J. Wind Eng. Ind. Aerodyn.*, **91**, 219–229, doi:10.1016/S0167-6105(02)00347-1.

Ulaby, F. T., and M. El-Rayes, 1986: Microwave dielectric spectrum of vegetation material. *Proceedings of the 1986 International Geoscience and Remote Sensing Symposium (IGARSS'86) on Remote Sensing: Today's Solutions for Tomorrow's Information Needs*, Vol. 2, ESA Publications Division, ESA SP-254, 1103–1106.

Vivekanandan, J., M. Politovich, R. Rilling, S. Ellis, and F. Pratte, 2004: Sensitivity of S- and Ka-band matched dual-wavelength radar system for detecting nonprecipitating cloud. *Microwave Remote Sensing of the Atmosphere and Environment IV*, G. Skofronick Jackson and S. Uratsuka, Eds., International Society for Optical Engineering (SPIE Proceedings, Vol. 5654), 14–24, doi:10.1117/12.581131.

Wakimoto, R. M., P. Stauffer, W.-C. Lee, N. T. Atkins, and J. Wurman, 2012: Finescale structure of the LaGrange, Wyoming, tornado during VORTEX2: GBVTD and photogrammetric analyses. *Mon. Wea. Rev.*, **140**, 3397–3418, doi:10.1175/MWR-D-12-00036.1.

Waterman, P. C., 1969: Scattering by dielectric obstacles. *Alta Freq.*, **38**, 348–352.

——, 1971: Symmetry, unitarity and geometry in electromagnetic scattering. *Phys. Rev.*, **3D**, 825–839, doi:10.1103/PhysRevD.3.825.

White, F. M., 1991: *Viscous Fluid Flow*. 2nd ed. McGraw-Hill Series in Mechanical Engineering, McGraw-Hill, 614 pp.

Wurman, J., and S. Gill, 2000: Finescale radar observations of the Dimmitt, Texas (2 June 1995), tornado. *Mon. Wea. Rev.*, **128**, 2135–2164, doi:10.1175/1520-0493(2000)128<2135:FROOTD>2.0.CO;2.

——, J. M. Straka, and E. N. Rasmussen, 1996: Fine-scale Doppler radar observations of tornadoes. *Science*, **272**, 1774–1777, doi:10.1126/science.272.5269.1774.